High Aspect Ratio WO_3 Nanostructures Anodically Grown in a Pure Molten o-H_3PO_4 Electrolyte and their use as H_2 Gas-sensors

by Marco Altomare,[1] Ole Pfoch,[1] Alexei Tighineanu,[1] Robin Kirchgeorg,[1] Kiyoung Lee,[1] Elena Selli[2] and Patrik Schmuki[1,3]*

[1] Department of Material Science and Engineering, WW4-LKO, University of Erlangen-Nuremberg, Martensstrasse 7, D-91058 Erlangen, Germany

[2] Department of Chemistry, University of Milan, Via C. Golgi 19, I-20133 Milan, Italy

[3] Department of Chemistry, King Abdulaziz University, Jeddah, Saudi Arabia

* Corresponding author Tel.: +49-9131-852-7575 Fax: +49-9131-852-7582
Email: schmuki@ww.uni-erlangen.de

A B S T R A C T

Layers of vertically aligned WO_3 nanochannels with individual pore diameter of *ca*. 10 nm are anodically grown in a pure molten ortho-phosphoric acid (o-H_3PO_4) electrolyte. For this, no addition of additives such as water, organics or other salts to the electrolyte is required. When converted into crystalline structures by proper thermal treatment, the anodic WO_3 nanochannel layers exhibit outstanding gas-sensing ability. These gas-sensors can be operated at relatively low temperature (80-120°C) and deliver fast response-recovery times, so to reliably detect H_2 traces with concentration as low as of *ca*. 500 ppb. The enhanced sensing ability is ascribed to the structural features of so-fabricated anodic films that are characterized by large surface area and one-dimensional morphology, allowing for fast and reproducible response even to H_2 traces in the ppb range.

Keywords: anodization, tungsten oxide, phosphoric acid, molten salt, hydrogen, gas-sensing

1. Introduction

Tungsten trioxide (WO_3) is an n-type semiconductor that has received large attention in the last decades in both scientific and technological fields due to its electronic and optical properties. It has been investigated as photocatalyst [1] and to fabricate electrodes for electrochromic devices [2] and for photo-electrochemical cells (*i.e.*, water splitting) [3]. In particular, after the pioneering work of P.J. Shaver in 1967 [4], WO_3 has been intensively studied also as gas sensor, mainly for H_2, H_2S and NO_x detection [5-7].

For resistive gas-sensors [8], the sensing mechanism is based on the change of semiconductor resistance upon exposure to a certain analyte. This is a surface phenomenon related to the extent of oxygen adsorption, and the larger the active surface of the semiconductor, the more pronounced is the sensor response to a given analyte (enhanced "receptor" function) [9]. Therefore, a large surface area is desired for the device and is typically obtained by fabricating gas-sensors from sintered oxide nanoparticle layers [10].

On the other hand, also the microstructure of the semiconductor largely affects the sensor performance ("transducer" function). In fact, it has been shown that improved sensitivities of the device are achieved by reducing the dimension of the oxide nanoparticles down to values comparable to the Debye length of the semiconductor, *i.e.*, the depth of the surface space charge layer [9]. When this occurs, the electron transport takes place through the space charge layer in the "necks" (*i.e.*, connectivities between adjacent crystallites), and the resistance of the device (and thus also the device sensitivity) becomes strictly related to the environment and hence gas-dependent.

Therefore, nanostructuring the semiconductor into one-dimensional (1D) architectures represents a potential key to fabricate functional oxide films and devices with improved performance [11].

Classical approaches to prepare nanostructured WO_3 films include sol-gel and hydrothermal processes that use alkoxides as starting material [12,13]. These lead to WO_3 nanoparticle slurries and post-treatments are needed to separate the oxide from the liquid phase so that the nanoparticles are then deposited (and sintered) on desired substrates for further use. Other frequently employed methods are spray pyrolysis [14], sputtering [15] and thermal or e-beam evaporation [16,17].

Besides, electrochemical anodization represents a simple, versatile and cost-effective approach for fabricating nanostructured oxide layers [18]. Electrochemical anodization has been extensively explored in the last decades to grow highly-ordered self-organized TiO_2 nanotube arrays [19] as well as many other morphologies and nanostructured metal oxides [20], this since an optimized anodization strategy allows for a fine control over the oxide structural features.

Concerning the growth of porous anodic WO_3 films, a limited number of attempts have been reported, this because anodization of tungsten leads in many electrolytes to soluble species [21-23] and, consequently, the control over the anodic oxide structure results challenging.

One of the first reports in such context is that of Mukherjee *et al*. [24], which describes the growth of nanoporous WO_3 films by galvanostatic oxidation of W foil in aqueous oxalic acid. However, these films were rather thin (*e.g.*, few tens of nm), while thicker layers are clearly desired for further applications.

Other follow-up studies reported on the use of aqueous NaF electrolytes though, also in these cases, the degree of self-ordering was rather poor and the layers were only 200-300 nm-thick [25,26].

The fabrication of 1D anodic WO_3 nanostructures, that is, high aspect ratio morphologies, was firstly reported by Hahn *et al*., who developed a strategy based on rapid anodic growth of WO_3 nanotube bundles in aqueous NaCl or $HClO_4$ electrolytes [27]. However, although nanotube bundles as long as 10-20 µm could be formed, these layers were not uniform as the anodic growth occurred through breakdown events that were randomly distributed over the anodized surface.

Subsequently, more uniform and stable WO_3 layers with several µm-long vertically-aligned nanochannels were fabricated, as reported by Wei *et al*. [28], in an NH_4F-containing ethylene glycol electrolyte. Interestingly, an electrolyte with limited water content (<0.2wt%) as the one used by Wei *et al*. is seemingly the key to form such thick regular nanostructures.

In this work we show a new anodization approach carried out in a hot pure o-H_3PO_4 electrolyte that leads to the formation of functional, high aspect ratio WO_3 layers. The growth conditions were optimized to fabricate thick ordered nanochannel structures. At the same time, we also address a critical aspect of using anodic layers grown on conductive (metallic) substrates as resistive gas-sensors, that is, the high electric conductivity of the substrate (*i.e.*, W foil) typically contributes to a significant drop of the device sensitivity, this because the current flows preferentially through the metallic foil, and the change of the anodic film resistance upon exposure to the analyte (*e.g.*, H_2) becomes negligible compared to the overall resistance of the device. Thus, to overcome this issue, we fabricate porous anodic layers by anodizing W films that are e-beam

evaporated onto non-conductive glass. These structures, which are converted into crystalline WO_3 by proper thermal treatment, exhibit very promising results when tested as H_2 gas-sensors. Reproducible and fast gas-sensing response along with high sensitivity is provided by the large surface area and 1D morphology of these anodic structures.

2. Results and Discussion

Fig. 1(a)-(f) show SEM and TEM images of the optimized WO_3 nanochannel layers that were grown on glass substrates by using the here introduced o-H_3PO_4-based anodization approach. As also shown in Fig. S1 and S2, this procedure leads to the growth of high aspect ratio pores with mean diameter of 10 nm (see).

Key factor to succeed in the growth of such ordered structure is the use of a hot pure o-H_3PO_4 electrolyte. Pure o-H_3PO_4 (*i.e.*, ortho-phosphoric acid) is solid at room temperature but melts at *ca*. 40°C. We found that when molten, a hot pure o-H_3PO_4 medium is suitable for the growth of anodic porous layers.

To achieve optimized self-ordering anodization conditions, a set of parameters was screened by performing preliminary experiments on W foil (see the ESI for experimental details). In particular, we observed that temperature and composition of the electrolyte, applied potential and anodization time were of relevant importance (results of preliminary experiments are summarized in Table S1 and S2).

Fig. S3 (see ESI) shows ordered WO_3 nanochannel structures that were grown on W foils by optimized anodization (pure o-H_3PO_4, 5 V, 100°C). The equilibrium between field-assisted passivation and oxide dissolution (that is a prerequisite for self-ordering anodization) is established only at an electrolyte temperature of *ca*. 100°C. At lower

temperature, a compact oxide or relatively thin porous layers were formed (Fig. S4). Thicker nanochannels could be formed at 120°C although these showed large extent of etching at the outermost part of the anodic film, most probably ascribed to fast oxide dissolution occurring at relatively high temperature.

We also found that an applied potential of 2.5-10 V was ideal to form thick and ordered WO_3 nanochannel layers. Current density (J) *vs*. time profiles were recorded when anodizing at these applied potentials (Fig. S5) and revealed that steady state J values as low as of 0.1-0.6 mA cm^{-2} are needed to establish a controlled oxide growth. Such profiles indicate that passivation firstly occurs (sudden increase and drop of J) which is followed by steady state condition, that is, a nearly constant J is reached, and desired equilibrium between metal passivation and oxide dissolution is obtained, leading to ordered structures as those shown in Fig. S6. On the contrary, only a few tens of nm-thick porous layer was formed at 1 V (the short thickness is in line with a J of few μA cm^{-2}), while potentials of 15 V or higher led to significantly less ordered nanochannel layers (in agreement with J values as high as of tens of mA cm^{-2}).

At the same time, similar results were obtained by performing experiments in galvanostatic conditions (Fig. S7). By setting J at *ca*. 1.2 mA cm^{-2} (such J value exceeds that observed when anodizing at 2.5-10 V but is lower than that measured at 15 V), we found that the potential, after a first increase up to *ca*. 9 V, stabilizes at 5-6 V, and highly ordered nanochannel structures were obtained that resembles those fabricated by the optimized potentiostatic approach.

Another key advantage of the here presented anodization process is that the electrolyte can be repeatedly used for anodizing with no detrimental effects on the anodic film morphology (see Table S1). However, it's worth noting that o-H_3PO_4 is

rather hygroscopic (especially when pure) and tends to uptake water from the environment. Thus, to investigate the effect of water, we firstly performed anodization experiments (optimized conditions) during which a little amount of water was added to the electrolyte (so to reach a nominal water content of *ca*. 0.5 vol%). The J-time profile of this experiment shows, corresponding to the instant of water addition, a sharp positive spike that indicates sudden acceleration of the oxide dissolution (Fig. S8). However, in a few minutes, J recovered to steady state values and the anodization experiments finally led to highly-ordered WO_3 nanochannel structures.

The role of water was further investigated by growing anodic films in o-H_3PO_4-based electrolytes with different initial water contents. While a water content of 2 vol% did not detrimentally effect the structure of the WO_3 film, larger amounts of water (*i.e.*, 10 vol%) led to dramatic increase of etching rate and consequently to less ordered porous films (see Fig. S8).

These results can be explained assuming that limited amounts of water rapidly evaporate from the hot o-H_3PO_4. Therefore, the electrolyte can be in principle recovered from water uptake by an extensive heating step prior to anodization. However we assume that even by using a hot anodizing medium, traces of water (most probably with concentration in the ppm range) are present and contribute as oxygen-source to the field-assisted W passivation. In line with the work of Wei *et al.* [28], such limited water content more probably represents the key to reach controlled growth of thick and ordered porous films.

Under optimized conditions, the thickening of the WO_3 layers was shown to follow a parabolic trend over the anodization time (Fig. S9). This is ascribed to the fact that for long anodization experiments, the outermost part of the film is exposed to the

electrolyte and therefore undergoes extensive etching (this is well in line with what observed for other anodically grown 1D oxides [29]). However, for relatively short experiments (*e.g.*, 0.5-8 h-long), we found that the layer thickness linearly increased over the anodization time with an average growth rate of *ca*. 0.25 μm h^{-1}, and, most importantly, these films showed straight nanochannels with top open pores.

Additional key strengths of the here presented approach are that *i)* the concept can be extended to the use of other phosphorus-containing acids, that is, hot pure pyro- and poly-phosphoric acids are suitable electrolytes for the growth of ordered anodic porous WO_3 structures (Fig. S10); and *ii)* hot pure o-H_3PO_4 can be effectively used also to anodically form Al_2O_3 nanopore (Fig. S11) and Nb_2O_5 nanochannel (Fig. S12) structures. Overall, these aspects clearly highlight the broad potential of this approach and its technological significance in view of fabricating advanced nanostructured materials.

The optimized anodization approach was used for fabricating gas-sensing devices (Scheme S1). Fir this, we anodized 600-700 nm-thick W layers that were evaporated on non-conductive glass slides (Fig. 1 and Fig. S1). Highly ordered porous oxide films with a thickness of *ca*. 1.3 μm were grown after *ca*. 4 h-long anodization experiments, in full agreement with the results of preliminary screening (Fig. 1(g)). The volume expansion is ascribed to the lower density of the metal oxide compared to that of the metal [30].

The complete conversion of metallic W into oxide film was shown to be another important key to fabricate functional devices (for more details see the ESI). For this, the J-time profiles were monitored during the anodization experiments and steady-state J values of 0.10-0.15 mA cm^{-2} were recorded that are well in line with those measured in

the preliminary experiments. We assumed the conversion of the metal film into porous oxide to be completed when J dropped to values of few μA cm^{-2} (Fig. 1(h)). This also occurred with gradual conversion of the film into a transparent oxide layer (Fig. 1(i)).

When as-formed, these anodic films were amorphous, as shown by XRD data, HRTEM image and SAED pattern in Fig. 2(a) and (c). Their conversion into crystalline structure was obtained by proper thermal treatment. We observed crystallization into monoclinic WO_3 by annealing at 350°C, as proved by appearance of intense reflections peaking at 23.2 and 23.7 degree (Fig. 2(b)) [24,26]. For layers annealed at 450°C we observed significantly more intense reflections, ascribed to higher degree of crystallinity. The crystallization of these layers was also confirmed by HRTEM as lattice planes of crystalline WO_3 were clearly visible (Fig. 2(d)). Also, the SAED pattern showed a four-fold symmetry with d spacing of 3.86, 2.70, 1.93 and 1.69 Å corresponding to the (002), (022), (004) and (042) planes of monoclinic WO_3 [31].

Interestingly, higher annealing temperature (≥550°C) led to formation of sodium tungstate species (these with different stoichiometry and crystallographic features) as proved by appearance of intense reflections mainly at 10.8, 24.3 and 28.3 degree (Fig. 2(b)) [32,33]. These results can be explained by assuming that at such high annealing temperature, solid state reaction occurs that leads to diffusion of Na ions from the glass substrate into the oxide film. This is in agreement with WO_3 crystallographic features and consequent ability to intercalate Na^+ ions [34]. Moreover, we also noticed that high temperature annealing led to significant sintering and collapse of the structures (Fig. S13), and to a change of the anodic film color (from transparent into pale yellow, that can be ascribed to partial WO_3 reduction due to Na^+ intercalation, *i.e.*, electrochromism,

or to formation of tungstate species). On the other hand, the nanochannel structures were shown to withstand thermal treatment at temperatures up to 450°C.

XPS analysis of both as-formed and annealed layers further confirmed the formation of WO_3 (Fig. 2(e)-(h)). Interestingly, the survey spectra of the film annealed at 450°C (Fig. 2(e)) showed intense Na1s signal. Once more, one can explain this assuming that the thermal treatment at 450°C enables Na ion intercalation. On the other hand, the film was shown to be composed of monoclinic WO_3 so that we assume that only higher annealing temperatures (≥550°C) enable intercalation of significant amounts of Na ions with consequent transformation of WO_3 into stoichiometric $Na_2W_2O_7$.

The high resolution XPS spectra showed that peak position of $W4f_{7/2}$ and $W4f_{5/2}$ for as-formed layers were at 36.71 and 38.91 eV, respectively (Fig. 2(f)), that well correspond to the literature [35]. After annealing at 450°C, we observed a *ca*. 0.5 eV-shift of W4f doublet towards lower binding energies. However, according to the literature, a shift toward higher binding energies is typically observed after annealing that is ascribed to complete oxidation of the anodic film to form stoichiometric WO_3 and also to a reduction of hydroxide species and water adsorbed at the oxide surface [36]. Therefore, a shift towards lower binding energies can be due to intercalation of Na ions, as above discussed, that induces partial reduction of WO_3 [35].

According to the literature, the O1s signals were deconvoluted into two peaks by Gaussian fitting (Fig. 2(g)). The main peaks, that are those at lower binding energies, are attributed to lattice oxygen, and, in line with literature on anodic WO_3 [35], were found to peak at 530.88 and 530.28 eV, respectively, for the as-formed and annealed films. On the other hand, the peaks at higher binding energies, *i.e.*, peaking at *ca*. 532.27-531.48 eV, are attributable to adsorbed hydroxide [35]. The Gaussian fitting of

these peaks revealed that the amount of adsorbed hydroxide species was of *ca*. 13% for both as-formed and annealed films.

XPS analysis revealed also the presence of P in both as-formed and annealed films, as indicated by the P2p signals peaking at 134.71 and 134.45 eV [35], respectively, corresponding to P concentration of *ca*. 1.2-1.4 at%. These results were found to be well in line with those provided by EDAX measurements, which revealed P contents of *ca*. 1.1-1.2 at% (Fig. S14) [27].

The value of the structures produced in this work was assessed by performing a series of H_2 gas-sensing experiments (see Scheme S2 and ESI for experimental details). The fabrication of the gas-sensing devices was completed by depositing two Pt electrodes on top of the anodic layers (Fig. S15). Overall, the results (see below) were well in line with the H_2 sensing mechanism reported in the literature [4-7]. Briefly, the sensing ability of WO_3 is ascribed to reduction of the sensor resistance upon exposure to H_2 (reducing gas). This occurs because H_2 undergoes oxidation by oxygen species adsorbed at the surface of the oxide forming water as final product ("receptor" function), and thus, the consumption of adsorbed oxygen leads to the increase of conductivity of the sensor ("transducer" function).

A preliminary set of experiments was performed on films annealed at different temperature to identify the optimal thermal treatment (Fig. 3(a)). The best response, in terms of both speed and magnitude, was obtained for samples annealed at 350-450°C, which showed fast resistance drop-recovery upon exposure to H_2 pulses. These devices, for H_2 injections of 2.3 ppm, delivered response of 29.9 and 23.4%, respectively. However, a thermal treatment at 450°C was preferred over that at 350°C since the former led to more stable gas-sensors, *i.e.*, devices crystallized at 350°C showed

significant baseline drift and unreliable response over extended experiments. On the other hand, devices annealed at higher temperatures (≥550°C) delivered slow resistance drop-recovery while the films treated at 250°C showed poor and unreliable response. These results correspond well with what observed by XRD and SEM analysis, that is, films annealed at temperature ≥550°C underwent sintering (significant loss of porosity) and conversion into tungstate species, while structures treated at 250°C resulted not crystalline (Fig. 2(a) and Fig. S13).

By means of further screening experiments, we found the sensors to deliver reliable signal also at relatively low sensing temperature (Fig. 3(b)). In fact, stable and reproducible response as high as of *ca*. 23% to H_2 injections of 2.3 ppm was measured at 80 and 120°C. However, for extended experiments at 80°C we observed resistance drift and slight loss of reproducibility of the response (clearly, lower temperature led to even less reliable signal). Besides, higher sensing temperature led to significant decrease of the sensor response (when operating at 200°C, *r* dropped down to *ca*. 10%).

The gas-sensing ability of the devices was highlighted especially when screening the sensor response to H_2 concentration as low as of *ca*. 500 ppb (Fig. 3(c)-(e)). It is worth noting that, according to the literature, such low H_2 concentration are typically detected with WO_3-based gas sensors only if high sensing temperatures (≥300°C) are adopted (thermal activation) or if the semiconductor is decorated with noble metal (Pt or Pd) nanoparticles (catalytic activation) [36,37]. Indeed, without undertaking any of these strategies, we measured with our gas-sensors consistent and reproducible response to repeated H_2 pulses with concentration in the 0.5-2.3 ppm range (Fig. 3(c)). Interestingly, we observed for these devices not only a promising resistance to fatigue (*i.e.*, stability

over long term measurements) but also a stabilization of sensor response after extended experiments, as shown in Fig. 3(d).

The response to H_2 pulses of 500 ppb was of *ca*. 5% and the device also showed, in such a low range of H_2 concentration, a linear correlation between the response and the amount of analyte (Fig. 3(e)), which is clearly a desirable feature for H_2-leak sensors.

3. Conclusions

With this work we introduced a new anodization approach that allows for the growth of different nanostructured metal oxide layers. We showed that hot phosphoric acids, when pure, are suitable electrolyte for the anodic growth of nanostructured functional materials. In particular, the growth of highly-ordered WO_3 nanochannel layers was optimized and these structures were used to fabricate gas-sensing devices that can be operated at low temperature and without costly noble metal nanoparticle decoration. So-fabricated devices showed outstanding sensing ability and delivered reliable response to H_2 concentrations as low as of *ca*. 500 ppb.

Acknowledgements

Ulrike Marten-Jahns is acknowledged for helping in the evaluation of the diffraction data. Helga Hildebrand and Dr. Anca Mazare are acknowledged for technical help and fruitful discussion on XPS data. Dr. Mirza Mackovic and Florian Niekiel are acknowledged for technical help in TEM analysis. The authors would also like to acknowledge the ERC, the DFG and the Erlangen DFG cluster of excellence EAM for

financial support. Dr. Marco Altomare and Prof. Elena Selli acknowledge financial support from MIUR through the 2009PASLSN PRIN project.

References

[1] R. Abe, H. Takami, N. Murakami, B. Ohtani, Pristine Simple Oxides as Visible Light Driven Photocatalysts: Highly Efficient Decomposition of Organic Compounds over Platinum-Loaded Tungsten Oxide, *J. Am. Chem. Soc*. **2008**, *130*, 7780-7781.

[2] S. K. Deb, Optical and photoelectric properties and colour centres in thin films of tungsten oxide, *Philos. Mag.* **1973**, *27*, 801-822.

[3] G. Hodes, D. Cahen, J. Manassen, Tungsten trioxide as a photoanode for a photoelectrochemical cell (PEC), *Nature* **1976**, *260*, 312-313.

[4] P. J. Shaver, Activated Tungsten Oxide Gas Detectors, *Appl. Phys. Lett*.**1967**, *11*, 255-257

[5] Z. Xu, J. F. Vetelino, R. Lec, D. C. Parker, Electrical properties of tungsten trioxide films, *J. Vac. Sci. Technol. A* **1990**, *8*, 3634-3638.

[6] M. Akiyama, J. Tamaki, N. Miura, N. Yamazoe, Tungsten Oxide-Based Semiconductor Sensor Highly Sensitive to NO and NO_2, *Chem. Lett*. **1991**, *20*, 1611-1614.

[7] D. J. Smith, J. F. Vetelino, R. S. Falconer, E. L. Wittman, Stability, sensitivity and selectivity of tungsten trioxide films for sensing applications, *Sensors Actuat. B Chem.* **1993**, *13-14*, 264-268.

[8] T. Seiyama, A. Kato, K. Fujiishi, M. Nagatani, A New Detector for Gaseous Components Using Semiconductive Thin Films, *Anal. Chem*. **1962**, *34*, 1502-1503.

[9] N. Yamazoe, New approaches for improving semiconductor gas sensors, *Sensors Actuat. B Chem.* **1991**, *5*, 7-19.

[10] S. R. Morrison, Semiconductor Gas Sensors, *Sensors Actuat.* **1982**, *2*, 329-341.

[11] A. Palacios-Padrós, M. Altomare, A. Tighineanu, R. Kirchgeorg, N. K. Shrestha, I. Díez-Pérez, F. Caballero-Briones, F. Sanza, P. Schmuki, Growth of ordered anodic SnO_2 nanochannel layers and their use for H_2 gas sensing, *J. Mater. Chem. A* **2014**, *2*, 915-920.

[12] B. B. Lakshmi, C. J. Patrissi, C. R. Martin, Sol-Gel Template Synthesis of Semiconductor Oxide Micro- and Nanostructures, *Chem. Mater*. **1997**, *9*, 2544-2550.

[13] P. Yang, D. Zhao, D. I. Margolese, B. F. Chmelka, G. D. Stucky, Generalized syntheses of large-pore mesoporous metal oxides with semicrystalline frameworks, *Nature* **1998**, *396*, 152-155.

[14] C. M. Ghimbeu, R. C. van Landschoot, J. Schoonman, M. Lumbreras, Tungsten trioxide thin films prepared by electrostatic spray deposition technique, *Thin Solid Films* **2007**, *515*, 5498-5504.

[15] G. Sberveglieri, L. Depero, S. Groppelli, P. Nelli, WO_3 sputtered thin films for NO_x monitoring, *Sensors Actuat. B Chem*. **1995**, *26*, 89-92.

[16] S.-H. Lee, H. M. Cheong, C. E. Tracy, A. Mascarenhas, D. K. Benson, S. K. Deb, Raman spectroscopic studies of electrochromic a-WO_3, *Electrochim. Acta* **1999**, *44*, 3111-3115.

[17] A. Antonaia, M. L. Addonizio, C. Minarini, T. Polichetti, M. Vittori-Antisari, Improvement in electrochromic response for an amorphous/crystalline WO_3 double layer, *Electrochim. Acta* **2001**, *46*, 2221-2227.

[18] K. Lee, A. Mazare, P. Schmuki, One-Dimensional Titanium Dioxide Nanomaterials: Nanotubes, *Chem. Rev*. **2014**, *114*, 9385-9454.

[19] P. Roy, S. Berger, P. Schmuki, TiO_2 Nanotubes: Synthesis and Applications, *Angew. Chem.* **2011**, *123*, 2956-2995; *Angew. Chem. Int. Ed*. **2011**, *50*, 2904-2939.

[20] D. Kowalski, D. Kim, P. Schmuki, TiO_2 nanotubes, nanochannels and mesosponge: Self-organized formation and applications, *Nano Today* **2013**, *8*, 235-264.

[21] A. Di Paola, F. Di Quarto, C. Sunseri, Anodic oxide films on tungsten - I. The influence of anodizing parameters on charging curves and film composition, *Corros. Sci.* **1980**, *20*, 1067-1078.

[22] A. Di Paola, F. Di Quarto, C. Sunseri, Anodic oxide films on tungsten - II. The morphology and dissolution of the films, *Corros. Sci*. **1980**, *20*, 1079-1085.

[23] C. Santato, M. Odziemkowski, M. Ulmann, J. Augustynski, Crystallographically Oriented Mesoporous WO_3 Films: Synthesis, Characterization, and Applications, *J. Am. Chem. Soc.* **2001**, *123*, 10639-10649.

[24] N. Mukherjee, M. Paulose, O. K. Varghese, G. K. Mor, C. A. Grimes, Fabrication of nanoporous tungsten oxide by galvanostatic anodization, *J. Mater. Res.* **2003**, *18*, 2296-2299.

[25] H. Tsuchiya, J. M. Macák, I. Sieber, L. Taveira, A. Ghicov, K. Sirotna, P. Schmuki, Self-organized porous WO_3 formed in NaF electrolytes, *Electrochem. Commun*. **2005**, *7*, 295-298.

[26] S. Berger, H. Tsuchiya, A. Ghicov, P. Schmuki, High photocurrent conversion efficiency in self-organized porous WO_3, *Appl. Phys. Lett*. **2006**, *88*, 203119, 1-3.

[27] R. Hahn, J. M. Macák, P. Schmuki, Rapid anodic growth of TiO_2 and WO_3 nanotubes in fluoride free electrolytes, *Electrochem. Commun*. **2007**, *9*, 947-952.

[28] W. Wei, S. Shaw, K. Lee, P. Schmuki, Rapid Anodic Formation of High Aspect Ratio WO_3 Layers with Self-Ordered Nanochannel Geometry and Use in Photocatalysis, *Chem. Eur. J.* **2012**, *18*, 14622-14626.

[29] D. Kim, A. Ghicov, P. Schmuki, TiO_2 Nanotube arrays: Elimination of disordered top layers ("nanograss") for improved photoconversion efficiency in dye-sensitized solar cells, *Electrochem. Commun*. **2008**, *10*, 1835-1838.

[30] K. Yasuda, P. Schmuki, Control of morphology and composition of self-organized zirconium titanate nanotubes formed in $(NH_4)_2SO_4/NH_4F$ electrolytes, *Electrochim. Acta* **2007**, *52*, 4053-4061.

[31] O. Loopstra, H. M. Rietveld, Further refinement of the structure of WO_3, *Acta Cryst. Sect. B* **1969**, *25*, 1420-1421.

[32] *Bull. Soc. Fr. Mineral. Cristallogr*. **1968**, *91*, 292.

[33] K. Okada, H. Morikawa, F. Marumo, S. Iwai, Disodium ditungstate, *Acta Cryst. Sect. B* **1975**, *31*, 1200-1201.

[34] J.-G. Zhang, D. K. Benson, C. E. Tracy, S. K. Deb, A. W. Czanderna, C. Bechinger, Chromic Mechanism in Amorphous WO_3 Films, *J. Electrochem. Soc*. **1997**, *144*, 2022-2026.

[35] B. Yous, S. Robin, A. Donnadieu, G. Dufour, C. Maillot, H. Roulet, C. Senemaud, Chemical vapor deposition of tungsten oxides: A comparative study by X-ray photoelectron spectroscopy, X-ray diffraction and reflection high energy electron diffraction, *Mater. Res. Bull*. **1984**, *19*, 1349-1354.

[36] H. Nakagawa, N. Yamamoto, S. Okazaki, T. Chinzei, S. Asakura, A room-temperature operated hydrogen leak sensor, *Sensors Actuat. B Chem.* **2003**, *93*, 468-474.

[37] S.J. Ippolito, S. Kandasamy, K. Kalantar-zadeh, W. Wlodarski, Hydrogen sensing characteristics of WO_3 thin film conductometric sensors activated by Pt and Au catalysts, *Sensors Actuat. B Chem.* **2005**, *108*, 154-158.

Figure captions

Figure 1 – (a,b) Top view and (c,d) cross sectional SEM images of WO_3 nanochannel layers grown on non-conductive glass substrates by optimized anodization (pure o-H_3PO_4, at 5 V, 100°C); (e,f) relative TEM images; (g,h) J-time profile recorded during the anodization experiment with (h) showing a magnified view of the same profile; (i) optical pictures of the so obtained porous transparent WO_3 nanochannel layer grown on non-conductive glass slide

Figure 2 – XRD, TEM and XPS characterization of *ca*. 1.3 µm-thick WO_3 nanochannel layers grown on non-conductive glass substrates by optimized anodization (pure o-H_3PO_4, at 5 V, 100°C), as-formed and annealed at different temperature (250-670°C range, air, 1 h). (a,b) XRD patterns of as-formed and annealed layers; (b) magnified view of 10-30 degree region of data shown in (a); (c,d) HRTEM images and SAED patterns (insets) of (c) as-formed and (d) annealed (450°C) films; (e-h) XPS data of as-formed and annealed (450°C) films showing (e) survey spectra and high resolution spectra in the (f) W4f, (g) O1s and (h) P2p regions. The lines with square and circle symbols in (g) are the experimental data, while the pink and blue curves are the two peaks determined by Gaussian fitting of the experimental data (the cyan lines are the fitting baselines).

Figure 3 – H_2 gas-sensing results (artificial air was used as carrier gas) measured with gas-sensors fabricated from films grown on non-conductive glass by optimized anodization and annealed at different temperature (250-650°C, air, 1 h). (a) Response of devices fabricated by different annealing conditions to H_2 injections of 2.3 ppm at a sensing temperature of 120°C; (b) response of a device annealed at 450°C to H_2 injections of 2.3 ppm at different sensing temperature (80-200°C); (c) response of a device annealed at 450°C to H_2 injections of different concentrations (500 ppb - 2.3 ppm) at a sensing temperature of 120°C; (d) stable response of a device annealed at 450°C to H_2 injections of 500 ppb at a sensing temperature of 120°C (data are taken

from the red box in (c)); (e) plot summarizing the response of a device annealed at 450°C to H_2 injections of different concentrations (500 ppb - 2.3 ppm) at a sensing temperature of 120°C.

Figure 1

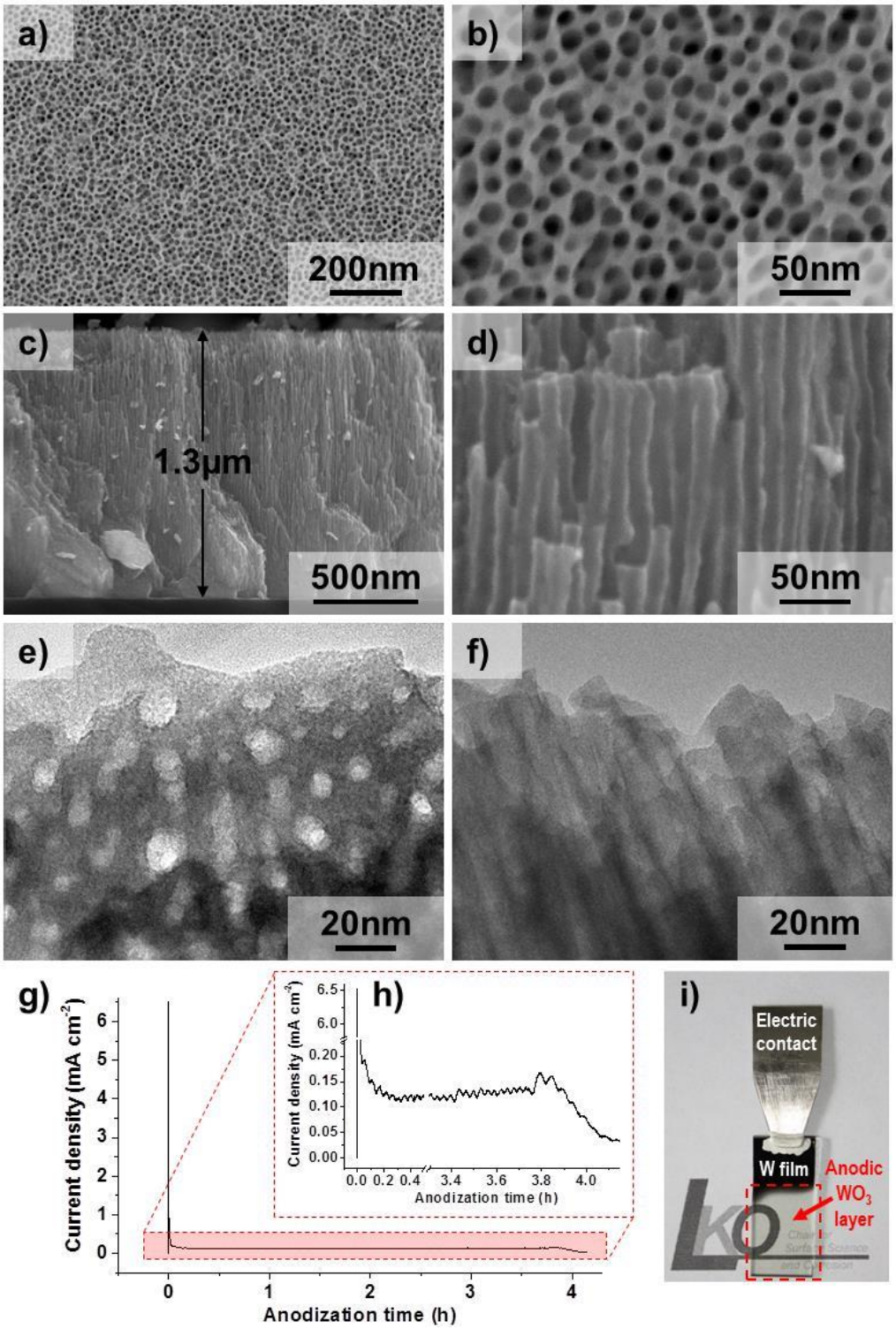
a)
200nm
b)
50nm
c)
1.3μm
500nm
d)
50nm
e)
20nm
f)
20nm
g)
Current density (mA cm-2)
Anodization time (h)
h)
Current density (mA cm-2)
Anodization time (h)
i)
Electric contact
W film
Anodic WO3 layer

Figure 2

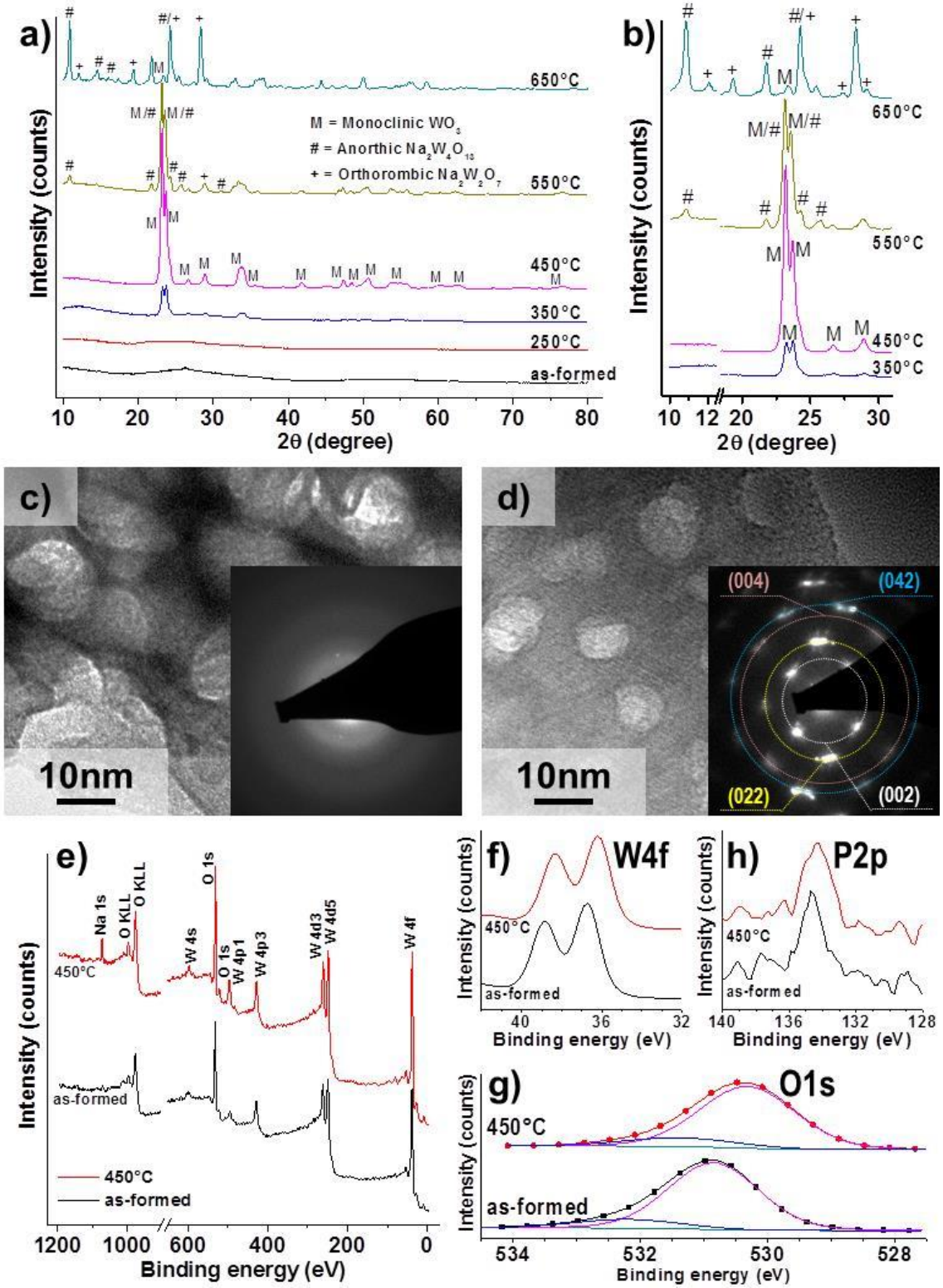
a)
b)
Intensity (counts)
2θ (degree)
650°C
550°C
450°C
350°C
250°C
as-formed
M = Monoclinic WO3
# = Anorthic Na2W4O13
+ = Orthorombic Na2W2O7
c)
d)
10nm
(004)
(042)
(022)
(002)
e)
Na 1s
O KLL
O 1s
W 4s
W 4p1
W 4p3
W 4d3
W 4d5
W 4f
Binding energy (eV)
f) W4f
h) P2p
g) O1s

Figure 3

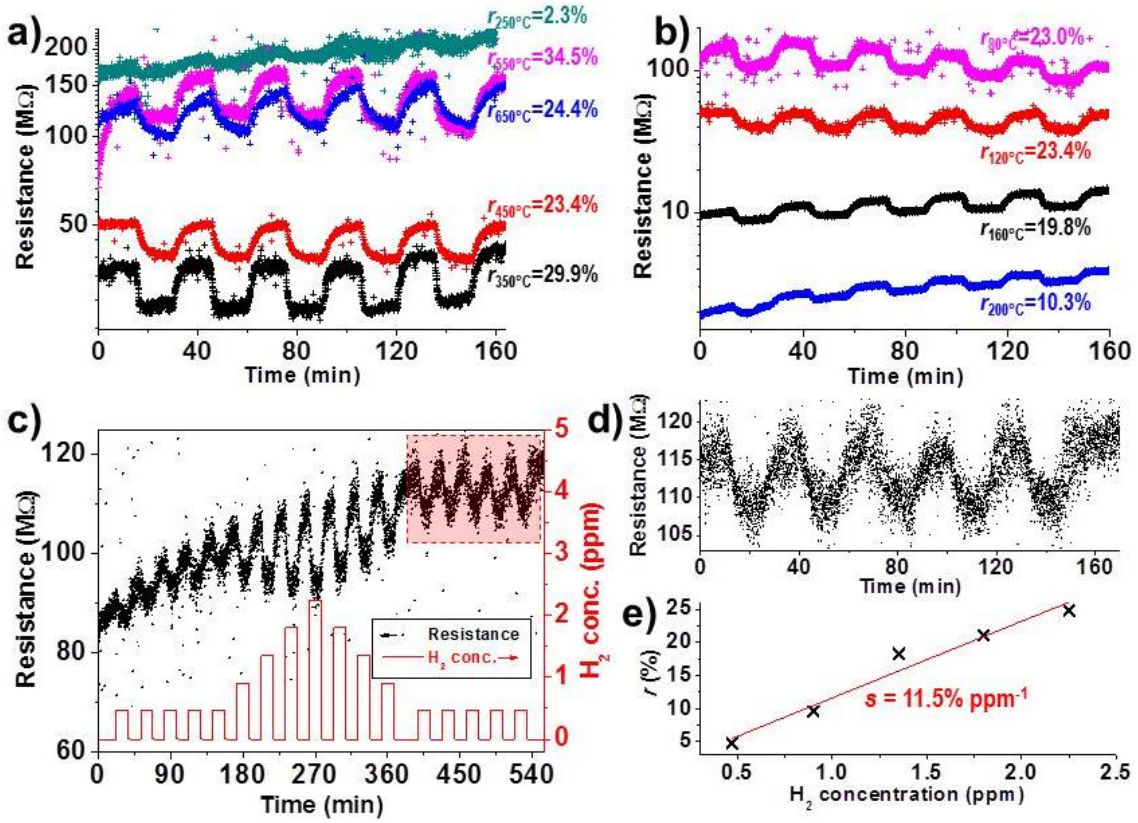
a)
Resistance (MΩ)
Time (min)
$r_{250°C}$=2.3%
$r_{550°C}$=34.5%
$r_{650°C}$=24.4%
$r_{450°C}$=23.4%
$r_{350°C}$=29.9%
b)
Resistance (MΩ)
Time (min)
$r_{80°C}$=23.0%
$r_{120°C}$=23.4%
$r_{160°C}$=19.8%
$r_{200°C}$=10.3%
c)
Resistance (MΩ)
H_2 conc. (ppm)
Time (min)
Resistance
H_2 conc.
d)
Resistance (MΩ)
Time (min)
e)
r (%)
H_2 concentration (ppm)
s = 11.5% ppm^{-1}